Research Square

Preprints are preliminary reports that have not undergone peer review.
They should not be considered conclusive, used to inform clinical practice,
or referenced by the media as validated information.

BRCA1 and 53BP1 Antagonistically Tune a Chromatin Compaction Gradient to Control DNA Break Mobility

Elizabeth Hinde

elizabeth.hinde@unimelb.edu.au

University of Melbourne https://orcid.org/0000-0001-8317-1152

Jieqiong Lou

university of melbourne

Julissa Sanchez Velasquez

University of Melbourne

Saul Menendez Cardenas

University of Melbourne

Ashleigh Solano

The Walter Eliza Hall Institute of Medical Research

Xiaomeng Zhang

University of Melbourne

Andrew Garvie

Monash University

Qihong Zhao

Peter MacCallum Cancer Centre

Lee Wong

Monash University https://orcid.org/0000-0002-4005-7330

Ian Campbell

Peter MacCallum Cancer Centre

Article

Keywords:

Posted Date: November 6th, 2026

DOI: https://doi.org/10.21203/rs.3.rs-10685534/v1

License: This work is licensed under a Creative Commons Attribution 4.0 International License.
Read Full License

Additional Declarations: There is **NO** Competing Interest.

BRCA1 and 53BP1 Antagonistically Tune a Chromatin Compaction Gradient to Control DNA Break Mobility

Jieqiong Lou[1,2], Julissa S. Velasquez[1], Saul M. Cardenas[1], Ashleigh N. Solano[3], Xiaomeng Zhang[1], Andrew Garvie[2], Qihong Zhao[4], Lee H. Wong[2], Ian G. Campbell[4,5], Elizabeth Hinde[1,6*]

1. School of Physics, The University of Melbourne, Parkville, Victoria 3010, Australia.
2. Department of Biochemistry and Molecular Biology, Biomedicine Discovery Institute, Monash University, Clayton, Victoria 3800, Australia.
3. The Walter and Eliza Hall Institute of Medical Research, Parkville, Victoria, Australia.
4. Research Division Peter MacCallum Cancer Centre, Melbourne, Victoria, Australia.
5. Sir Peter MacCallum Department of Oncology, University of Melbourne, Melbourne, Victoria, Australia.
6. School of Chemistry, The University of Melbourne, Parkville, Victoria 3010, Australia.

*Corresponding author email: elizabeth.hinde@unimelb.edu.au

Abstract

The two principal DNA double-strand break (DSB) repair pathways impose fundamentally different mechanical requirements on damaged chromatin. Non-homologous end joining (NHEJ) confines broken DNA ends to preserve their proximity, whereas homologous recombination (HR) requires damaged chromatin to become sufficiently mobile for homology search. While breast cancer associated gene 1 (BRCA1) and p53 binding protein 1 (53BP1) are established molecular regulators of DSB repair pathway choice, the chromatin architecture that translates this choice into the required mechanical state of the break has remained undefined. Here, we developed a multiplexed live-cell imaging framework combining phasor-based fluorescence lifetime imaging microscopy of histone Förster resonance energy transfer (FLIM-FRET) with single-particle tracking (SPT) of fluorescently labelled DSB repair proteins, enabling nanoscale chromatin compaction to be directly correlated with the mobility of individual DSBs in living cells. We show that DSB induction generates a chromatin compaction gradient between locally de-compacted repair sites and the surrounding compact chromatin. This gradient regulates DSB mobility, with HR-associated breaks exhibiting steeper gradients, increased mobility and greater exploration of the nuclear space than NHEJ-associated breaks, which remain spatially confined. BRCA1 and 53BP1 antagonistically regulate this gradient: BRCA1 promotes chromatin opening and restrains DSB mobility, whereas 53BP1 drives compaction and enhances movement. Loss of BRCA1 collapses this balance, causing chromatin over-compaction and DSB hyper-mobility that collectively drive poly(ADP-ribose) polymerase (PARP) inhibitor-induced chromosome mis-joining, a phenotype rescued by 53BP1 depletion. Together, our findings identify the chromatin compaction gradient as a biophysical regulator of DSB mobility that fulfils the distinct mechanical requirements of HR and NHEJ, providing a mechanistic basis for PARP inhibitor sensitivity and resistance in BRCA1-deficient cancers.

Introduction

Genome integrity is continually challenged by DNA-damaging agents arising from endogenous metabolism and environmental stress. Among all forms of DNA damage, double-strand breaks (DSBs) are the most cytotoxic: a single unrepaired DSB can trigger chromosomal rearrangements, genomic instability, tumorigenesis, or cell death (*1*). To safeguard the genome, eukaryotic cells deploy two principal repair pathways: the rapid but error-prone non-homologous end joining (NHEJ), active throughout the cell cycle, and the high-fidelity homologous recombination (HR), restricted to S and G2 phases when a sister chromatid is available as a repair template (*2-5*). These pathways impose fundamentally different physical requirements on the damaged locus; NHEJ must confine broken ends in close proximity to prevent illegitimate rejoining, while HR requires the damaged site to undergo resection and conduct a search for a homologous sequence elsewhere in the nucleus. The antagonistic interplay between breast cancer associated gene 1 (BRCA1) and p53 binding protein 1 (53BP1) is well established as a molecular switch governing this choice: 53BP1 suppresses DNA-end resection to favour NHEJ, while BRCA1 displaces 53BP1 to permit resection and commit the break to HR (*6-15*). However, how the physical state of the chromatin fibre itself (*16*), independent of canonical signalling, contributes to meeting these distinct mechanistic demands and thereby influences DSB repair outcome remains poorly understood (*17-22*).

One key physical property of chromatin remodelled following DSB induction is its local compaction state, which is known from optical microscopy studies to regulate DSB repair factor localisation and dynamics across multiple spatial scales (*23-29*). For example, at the micrometre scale, live-cell microscopy of photoactivatable fluorescent protein (FP)-tagged histones has revealed a biphasic chromatin response to laser-induced DSBs involving an initial local expansion followed by compaction (*30-35*), while fluorescence correlation spectroscopy (FCS) of FP-tagged repair factor diffusion at DSB sites has shown that this chromatin remodelling event differentially modulates repair factor access to the damaged DNA template (*36-38*). At the nanoscale, phasor-based fluorescence lifetime imaging microscopy (FLIM) of Förster resonance energy transfer (FRET) between FP-tagged nucleosomes has demonstrated that laser- and restriction enzyme-induced DSBs generate a compact chromatin border that promotes repair factor accumulation at the lesion, and that BRCA1-marked DSBs occupy a more open local chromatin state than 53BP1-marked DSBs (*39, 40*), the latter being associated by super-resolution microscopy with a higher-order microdomain structure that restrains DNA-end resection (*41*). Together, these studies demonstrate that chromatin compaction regulates DSB site access, and that this physical property is distinct at DSBs marked for NHEJ versus HR. This in turn raises the question of how, and to what extent, this compaction difference shapes the mechanism by which these two competing repair pathways operate.

Beyond compaction state, local mobility is another biophysical property of chromatin known to be altered following DSB induction and to regulate DSB repair outcome (*42-50*). In particular, single-particle tracking (SPT) microscopy of a FP tagged repetitive DNA array in yeast first established that DSB formation, which disrupts chromosomal continuity, increases both local and global chromatin mobility to facilitate homology search during HR (*51, 52*), while in mammalian cells, although the magnitude of this enhancement remains debated (*49, 53*), substantial evidence indicates that damaged chromatin is more mobile than undamaged regions (*19, 54-59*). Mechanistically, this enhanced mobility is regulated by DSB repair proteins (*52, 54, 55, 57, 60-64*), chromatin remodellers (*65-67*), and cytoskeletal networks (*57, 68-71*). Notably, 53BP1 has been shown to be required for DSB mobility enhancement, with evidence suggesting that cytoskeletal forces are transmitted to the damaged chromatin locus to drive movement (*57*). Together, these studies demonstrate that DSB-induced chromatin mobility is a regulated physical response, governed by an interplay between DSB repair

proteins and intracellular architecture. Yet whether the distinct chromatin compaction environments of NHEJ and HR sites translate into different mobility regimes, and whether the antagonistic activities of BRCA1 and 53BP1 enforce this difference to dictate repair pathway mechanism, remains entirely unknown.

To determine whether the distinct chromatin compaction environments of NHEJ and HR sites translate into different DSB mobility regimes; and to investigate the role of BRCA1 and 53BP1 in enforcing this difference; we developed a multiplexed fluorescence microscopy framework coupling phasor-based FLIM of FRET between fluorescently tagged nucleosomes with SPT of fluorescently tagged DSB repair factors in the DSB inducible via AsiSI (DIvA) cell system, enabling spatiotemporal maps of nuclear-wide chromatin compaction at the level of nucleosome proximity to be correlated with the mobility of individual DSBs marked for NHEJ or HR. Using this approach, we reveal in live human cells that the chromatin compaction gradient between the nucleoplasm and a DSB site is correlated with local DSB mobility; HR-associated DSBs reside in more open chromatin, exhibit a steeper compaction gradient, and move further, while NHEJ-associated DSBs reside in more compact chromatin, exhibit a shallower gradient, and are spatially confined. We further show that BRCA1 and 53BP1 antagonistically regulate this gradient: BRCA1 promotes chromatin opening and restrains DSB mobility, whereas 53BP1 drives compaction and enhances movement. Loss of BRCA1 collapses this balance, producing excessive chromatin compaction and aberrantly high DSB mobility that collectively drive chromosome mis-joining under poly(ADP-ribose) polymerase (PARP) inhibitor treatment, an effect reversed by co-depletion of 53BP1. Together, these findings uncover a chromatin compaction-dependent mechanism of DSB mobility control that fulfils the distinct mechanical requirements of HR and NHEJ, and that underlies therapeutic sensitivity in BRCA1-deficient cancers.

Results

The NHEJ versus HR chromatin compaction gradient differentially regulates DSB mobility. To directly investigate the relationship between local chromatin compaction and DSB mobility, we developed a multiplexed microscopy framework combining phasor-based FLIM of FRET between H2B-eGFP (donor) and H2B-mCherry (acceptor) labelled nucleosomes with SPT of Halo-JF646 tagged DSB repair proteins, in the DIvA cell system (which harbours a 4-OHT-inducible AsiSI restriction enzyme that generates approximately 100 site-specific DSBs throughout the genome upon nuclear translocation of AsiSI following 4-OHT treatment) (*72, 73*). In this framework, phasor FLIM of nucleosome FRET provides a nuclear-wide readout of nanoscale chromatin compaction, in which the fluorescence lifetime of H2B-eGFP is quenched as a function of its proximity to H2B-mCherry on a scale of 1–10 nm (*39, 40*), while SPT of the Halo646-tagged repair proteins provides a local readout of damaged chromatin mobility, in which individual DSB foci are tracked frame-by-frame to extract diffusion coefficients (*57, 74*). To enable this multiplexed microscopy framework, DIvA cells were transiently transfected with H2B-eGFP, H2B-mCherry, and either HaloJF646-53BP1 or HaloJF646-PALB2 to mark NHEJ- and HR-associated DSBs respectively; partner and localiser of BRCA2 (PALB2) was selected as the HR marker since fluorescent tagging of PALB2 does not perturb its recruitment to DSBs or its HR function (*75, 76*). The transfected DIvA cells were then incubated with 4-OHT for 1 hour to induce DSBs, and those cells co-expressing all three constructs with 5–10 DSBs in the imaging plane were selected for subsequent FLIM-FRET and SPT data acquisition.

In each selected DIvA cell, FLIM maps of nucleosome FRET and SPT movies of DSB mobility were acquired in an interleaved scheme across a 1-hour imaging window. In each cycle, a FLIM map was first acquired in the H2B-eGFP channel with sufficient photon counts to resolve donor lifetime quenching due to FRET (our readout of nanoscale chromatin compaction) (**Fig. S1,**

S2), followed by a time-lapse movie in the JF646-DSB repair factor channel with sufficient spatiotemporal resolution to track individual DSB foci frame-by-frame (**Fig. S3**). This yielded 12 FLIM maps and SPT movies at 5-minute intervals per cell. For correlative analysis, nuclear drift and rotation correction indices derived from the initial intensity frame of each SPT movie (see Methods) were applied to the corresponding FLIM of FRET maps to align DSB dynamics and chromatin compaction at the same nuclear sites over time (**Fig. 1A–B**; additional full-time series in **Fig. S4**). Then at the single-DSB level, the x–y coordinates of newly formed, persistent foci identified by 53BP1-JF646 or PALB2-JF646 intensity and tracked across multiple SPT movies, were co-registered with the local fraction of pixels undergoing FRET in their corresponding FLIM maps, and the trajectory from each SPT movie plotted for mean square displacement (MSD) analysis to extract diffusion characteristics of each DSB (**Fig. 1C–D; Fig. S3**). For each retained DSB, three parameters were monitored at 5-minute intervals: mean JF646 intensity of 53BP1 or PALB2; local FRET pixel fraction; and DSB diffusion coefficient (**Fig. 1E-F;** more representative examples in **Fig. S4**); enabling chromatin compaction and mobility to be correlated over time at NHEJ- and HR-associated DSBs (**Fig. 1G–H**).

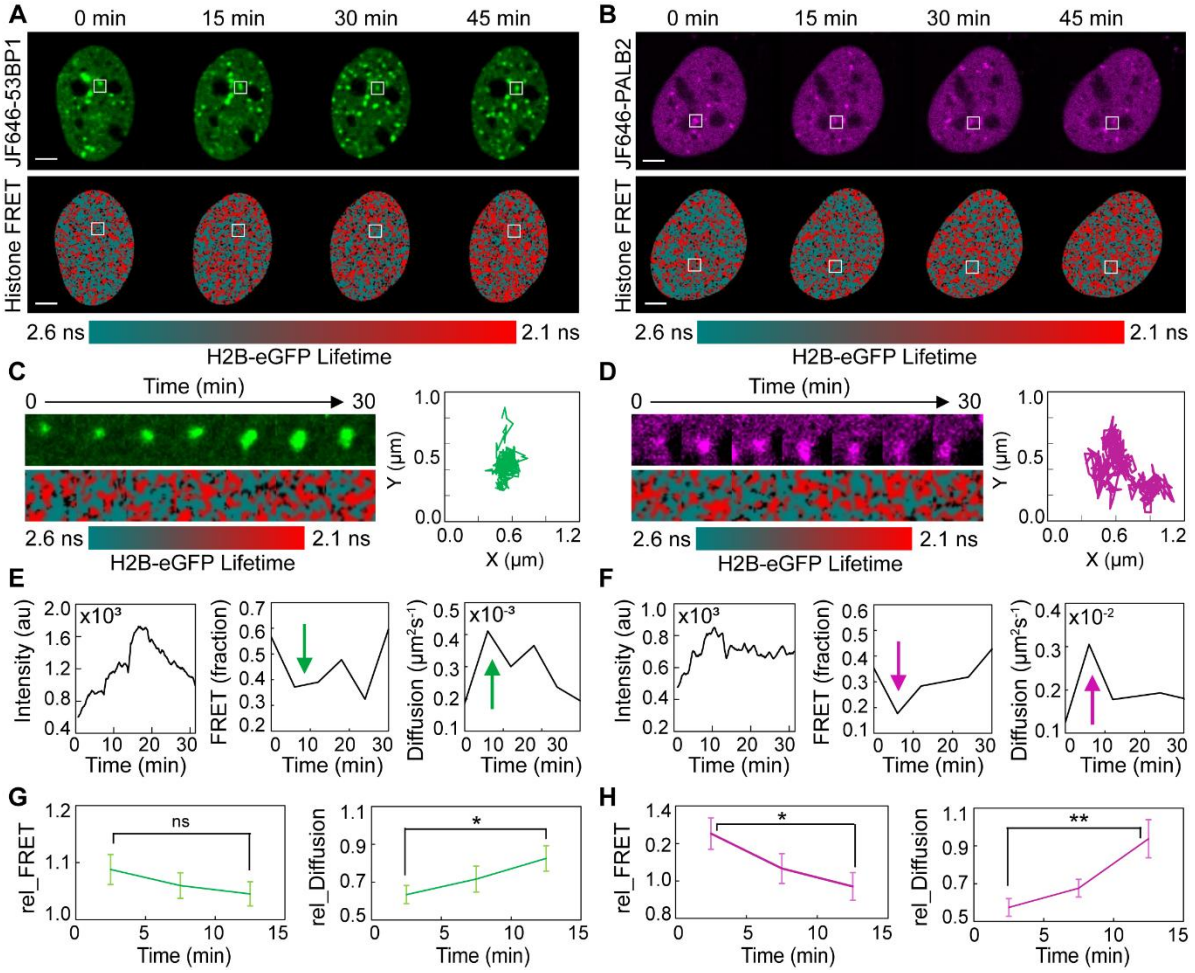


Figure 1. Multiplexed histone FRET and SPT reveal that chromatin opening at DSB sites correlates with increased DSB mobility. A-B. Time-lapse intensity images of HaloJF646-53BP1 (A) versus HaloJF646-PALB2 (B**)** following 4-OHT treatment (top), and the corresponding H2B-eGFP lifetime maps that report histone FRET with H2B-mCherry (red pixels = FRET, teal pixels = no FRET) (bottom). Scale bar: 5 μm. **C-D.** Zoomed-in images of the white boxed region in panel A-B (left) alongside HaloJF646 marked DSB trajectory for MSD analysis (right). **E-F.** Quantification of mean HaloJF646-53BP1 (E) versus HaloJF646-PALB2 intensity (left), H2B-eGFP and H2B-mCherry FRET fraction (middle), and DSB diffusion coefficient (right) over time for the foci shown in panel C-D (arrows indicate loss of histone FRET correlating with increase in DSB diffusion). **G-H.** Relative

change in histone FRET (left) versus DSB diffusion (right) at multiple HaloJF646-53BP1 (G) versus HaloJF646-PALB2 (H) foci. In G-H error bars represent SEM and for 53BP1 n = 189 foci from 13 cells (5 independent experiments) while for PALB2 n = 107 foci from 11 cells (4 independent experiments). ns $P > 0.05$, * $P < 0.05$, ** $P < 0.01$, t-test.

Visual inspection of the single-DSB multiparameter analysis (**Fig. 1E-F**) revealed that, for both 53BP1- and PALB2-positive DSBs, local chromatin opening; evidenced by a reduction in the FRET pixel fraction; coincided with an increase in the diffusion coefficient of DSBs within 15 minutes after repair protein recruitment **(Fig. 1G–H, Fig. S5**). Notably, this effect was more pronounced at PALB2-positive DSBs, suggesting that HR-associated DSBs are more mobile than those repaired by NHEJ. To directly confirm this, we co-transfected DIvA cells with eGFP-53BP1 and HaloJF646-PALB2, enabling simultaneous SPT of both DSB populations within the same cell (**Fig. 2A–B**), and a trajectory MSD analysis confirmed that PALB2-positive DSBs exhibit significantly higher diffusion coefficients than 53BP1-positive DSBs ($D_{PALB2} = 1.9 \times 10^{-3}$ versus $D_{53BP1} = 1.0 \times 10^{-3}$ μm²/s; **Fig. 2C–D**), consistent with HR-associated breaks being more mobile than those undergoing NHEJ. To then understand the nuclear-wide chromatin basis of this difference, a masked FLIM of nucleosome FRET analysis in DIvA cells co-transfected with H2B-eGFP, H2B-mCherry, and either HaloJF646-53BP1 or HaloJF646-PALB2 (**Fig. 2E–G**) revealed DSB induction to trigger global chromatin compaction; evidenced by an increase in the nuclear FRET pixel fraction (**Fig. S6**)(*40*); which, coupled with local chromatin opening at break sites, establishes a compaction gradient between the surrounding nucleus and each DSB. Normalising the local FRET pixel fraction at each DSB to the nuclear mean (where values < 1 indicate more open chromatin than the nuclear average) revealed this gradient to be significantly steeper at PALB2- versus 53BP1-positive DSBs ($norm_FRET_{PALB2} = 0.70 \pm 0.25$ versus $norm_FRET_{53BP1} = 0.97 \pm 0.17$; **Fig. 2H**), suggesting that this broader chromatin compaction context contributes to the enhanced mobility of HR-associated breaks.

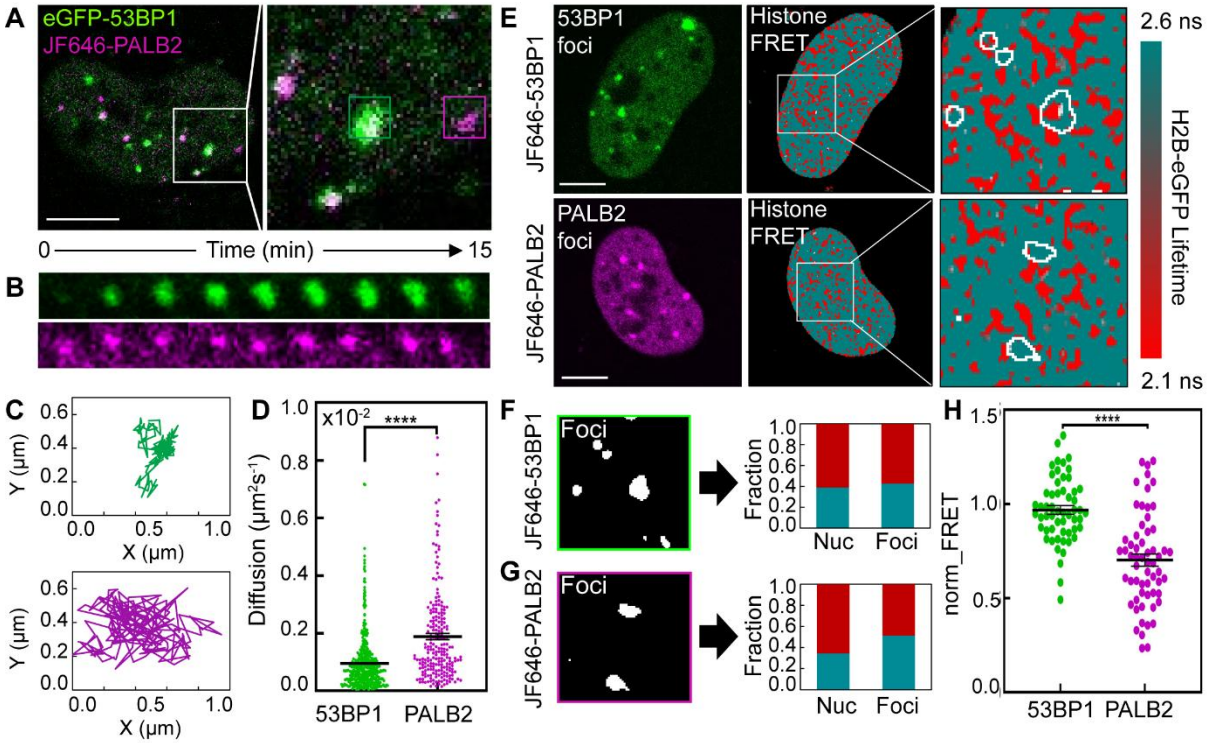


Figure 2. HR-associated DSBs are more mobile and sit in a steeper chromatin compaction gradient than NHEJ-associated DSBs. A. Merged intensity image (left) and zoomed-in region (right) of eGFP-53BP1 and HaloJF646-PALB2 in DIvA cells 1 hour after 4-OHT treatment. Scale bar: 5 μm.

B. Zoomed-in images of the green and magenta boxed regions in panel A as a function of time. **C**. X–Y trajectories of eGFP-53BP1 (top) and HaloJF646-PALB2 (bottom) positive DSBs shown in panel A-B, tracked over 16 minutes (200 frames, 5 s/frame). **D.** Quantification of DSB diffusion coefficients for eGFP-53BP1 versus HaloJF646-PALB2 positive DSB trajectories. In D error bars represent SEM and for 53BP1 n = 456 trajectories while for PALB2 n = 228 trajectories, from n = 9 cells across 2 independent experiments. **E.** Intensity images (left) of HaloJF646-53BP1 (top) versus HaloJF646-PALB2 (bottom) in DIvA cells 1 hour after 4-OHT treatment, and the corresponding H2B-eGFP lifetime maps that report histone FRET with H2B-mCherry (red pixels = FRET, teal pixels = no FRET) (middle), with the region of interests containing HaloJF646-marked foci traced in white. Scale bar: 10 μm. **F-G.** Representative examples of HaloJF646-marked masks enabling quantification of the fraction of pixels exhibiting histone FRET versus no FRET throughout the nucleoplasm (Nuc) and inside of DSBs (Foci) marked by 53BP1 (F) versus PALB2 (G). **H**. Normalisation of the fraction of histone FRET inside each DSB against the nucleoplasm across multiple cells. For 53BP1 n = 56 cells while for PALB2 n = 60 cells (3 independent experiments). The box and whisker plots show the minimum, maximum and sample mean. **** $P < 0.0001$, t-test.

BRCA1 and 53BP1 antagonistically regulate chromatin compaction and DSB mobility. Having established a link between the chromatin compaction gradient and differential DSB mobility at NHEJ and HR sites, we next sought to determine which molecular factors govern this gradient. The antagonistic interplay between BRCA1 and 53BP1 is well established as a molecular switch governing repair pathway choice, and we have previously shown that ring finger protein 8 (RNF8); an E3 ubiquitin ligase essential for the recruitment of both 53BP1 and BRCA1; is required for chromatin compaction following laser-induced DSBs (*39*), while BRCA1 is known to promote chromatin decompaction (*77*). We therefore hypothesised that BRCA1 and 53BP1 might antagonistically regulate the chromatin compaction gradient at DSB sites, and that this in turn underlies the distinct mobility regimes of NHEJ- and HR-associated breaks. To test this in DIvA cells, we knocked down 53BP1 ($DIvA^{53BP1\text{-}KD}$), BRCA1 ($DIvA^{BRCA1\text{-}KD}$), or both ($DIvA^{53BP1+BRCA1\text{-}KD}$) **(Fig. S7)**, and assessed the effect on: (1) chromatin compaction, by co-transfecting H2B-eGFP and H2B-mCherry and quantifying nuclear-wide FRET before and after DSB induction (**Fig. 3A–B**); and (2) DSB mobility, by co-expressing an eGFP tagged and truncated mutant of 53BP1 (eGFP-$53BP1_{1220–1711}$), which localises to DSBs without rescuing or interfering with endogenous 53BP1 function(*55*), alongside HaloJF646-PALB2, enabling simultaneous SPT of NHEJ- and HR-associated DSBs across all conditions (**Fig. 3C–D**). Consistent with our hypothesis, 53BP1 and BRCA1 antagonistically regulated both readouts. For chromatin compaction, DSB induction increased the global FRET pixel fraction by 25% in control cells, consistent with our earlier observation that DSBs trigger nuclear-wide chromatin compaction; this response was abolished in $DIvA^{53BP1\text{-}KD}$, further elevated in $DIvA^{BRCA1\text{-}KD}$ (36% increase), and non-significantly increased in $DIvA^{53BP1+BRCA1\text{-}KD}$ (**Fig. 3B**). For DSB mobility, $DIvA^{53BP1\text{-}KD}$ significantly reduced the mobility of both $53BP1_{1220–1711}$- and PALB2-positive DSBs, indicating that 53BP1 promotes chromatin mobility at both NHEJ and HR sites, while $DIvA^{BRCA1\text{-}KD}$ significantly increased $53BP1_{1220–1711}$-positive DSB mobility compared to control cells, demonstrating that BRCA1 restrains chromatin mobility during NHEJ. Critically, $DIvA^{53BP1+BRCA1\text{-}KD}$ restored the mobility of both DSB populations to baseline levels (**Fig. 3D**), confirming that the opposing activities of BRCA1 and 53BP1 jointly enforce the chromatin mobility regime at both repair sites.

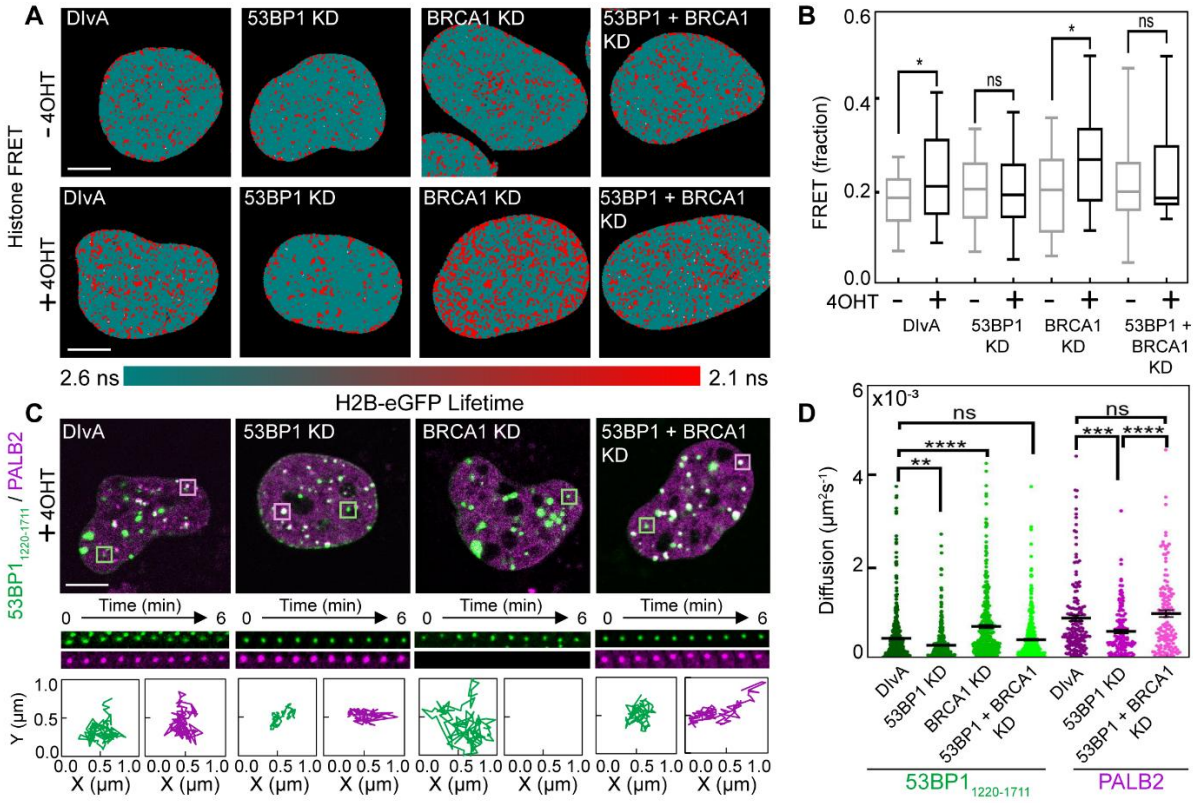


Figure 3. BRCA1 and 53BP1 antagonistically regulate chromatin compaction and DSB mobility. **A.** H2B-eGFP lifetime maps that report histone FRET with H2B-mCherry (red pixels = FRET, teal pixels = no FRET) in DIvA control, DIvA$^{53BP1\text{-}KD}$, DIvA$^{BRCA1\text{-}KD}$ and DIvA$^{53BP1+BRCA1\text{-}KD}$ cells before and 1 hour after 4-OHT treatment. Scale bar: 5 μm. **B.** Quantification of the fraction of pixels exhibiting histone FRET (indicative of compact chromatin) across multiple cells under the same conditions as in panel A. n ≥ 13 cells from 3 independent experiments. The box and whisker plots show the minimum, maximum and sample mean. ns $P > 0.05$, * $P < 0.05$, t-test. **C.** Merged intensity images of eGFP-53BP1$_{1220–1711}$ and HaloJF646-PALB2 in DIvA control, DIvA53BP1-KD, DIvABRCA1-KD and DIvA53BP1+BRCA1-KD cells 1 hour after 4-OHT treatment (top row), zoomed-in images of the green and magenta boxed regions in panel C as a function of time (middle row), and the corresponding X–Y trajectories of eGFP-53BP1$_{1220–1711}$ (green) versus HaloJF646-PALB2 (magenta) positive DSBs, tracked over 8 minutes (100 frames, 5 s/frame) (bottom row). Scale bar: 5 μm. **D.** Quantification of DSB diffusion coefficients for eGFP-53BP1$_{1220–1711}$ versus HaloJF646-PALB2 positive DSB trajectories. In D error bars represent SEM and DSB trajectory counts from left to right are 514, 418, 387, 416, 167, 136 and 144 from n ≥ 13 cells across 3 independent experiments. ns $P > 0.05$, ** P < 0.01, *** P < 0.001, **** P < 0.0001, one-way ANOVA.

To validate these findings in a physiologically relevant context, we generated BRCA1 knockout cells (MCF10A$^{BRCA1\text{-}KO}$) in the human breast epithelial cell line MCF10A and knocked down 53BP1 in this background (MCF10A$^{BRCA1\text{-}KO+53BP1\text{-}KD}$), then measured chromatin compaction and DSB mobility in MCF10A, MCF10A$^{BRCA1\text{-}KO}$, and MCF10A$^{BRCA1\text{-}KO+53BP1\text{-}KD}$ cells before and after treatment with the radiomimetic agent neocarzinostatin (NCS) (**Fig. 4A–B**). Consistent with observations in DIvA cells, NCS treatment promoted global chromatin compaction in MCF10A cells, and BRCA1 loss drove excessive compaction and significantly increased DSB mobility compared to MCF10A (**Fig. 4C**). Co-depletion of 53BP1 in MCF10A$^{BRCA1\text{-}KO}$ cells (MCF10A$^{BRCA1\text{-}KO+53BP1\text{-}KD}$) prevented chromatin over-compaction and fully restored DSB mobility to MCF10A levels (**Fig. 4A–C**), confirming that the hyper-mobility phenotype in BRCA1-deficient cells is 53BP1-dependent. This hyper-mobility was frequently accompanied by fusion of neighbouring DSB foci (**Fig. 4D**). To assess the functional consequence of this DSB hyper-mobility, MCF10A· MCF10A$^{BRCA1\text{-}KO}$, and MCF10A$^{BRCA1\text{-}$

$^{KO+53BP1-KD}$ cells were treated with the PARP inhibitor Olaparib (2 μM, 16 hours) and chromosome mis-rejoining quantified by mitotic spread assay (**Fig. 4E–F**). BRCA1 deficiency significantly increased chromosome mis-rejoining under Olaparib treatment, and co-depletion of 53BP1 mitigated this effect, reducing mis-rejoining to MCF10A levels, demonstrating that the chromosomal instability and PARP inhibitor sensitivity of BRCA1-deficient cells is driven by 53BP1-dependent DSB hyper-mobility.

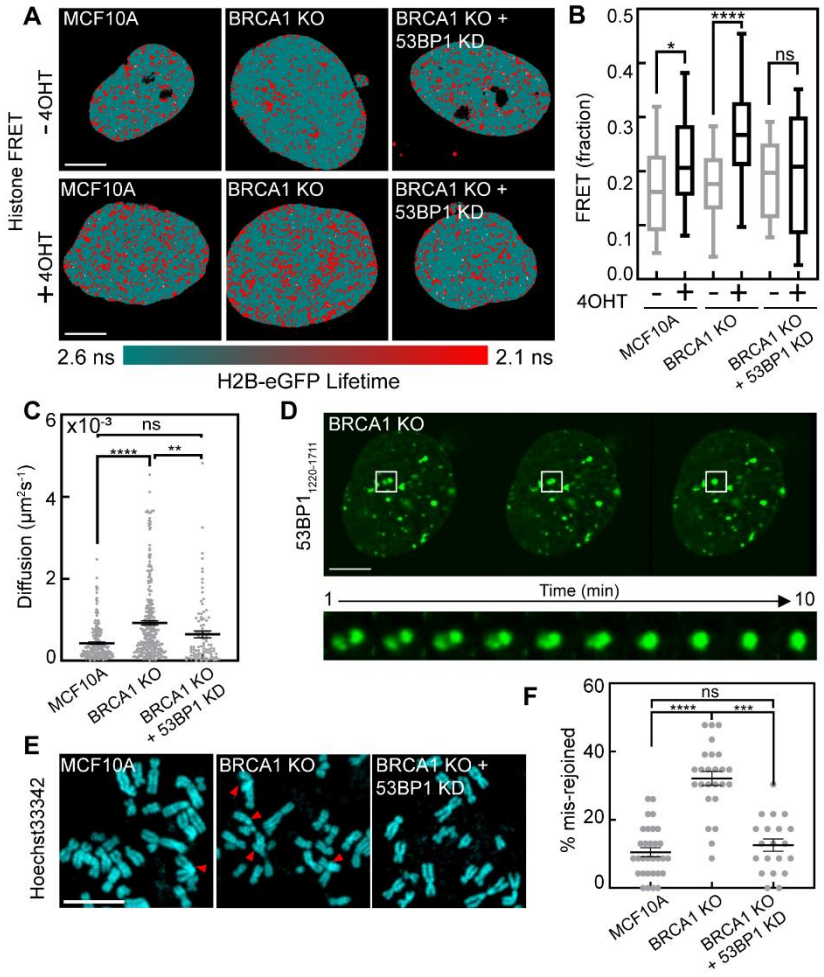


Figure 4. BRCA1 loss drives chromatin over-compaction and DSB hyper-mobility, promoting chromosomal mis-rejoining under PARP inhibition. A. H2B-eGFP lifetime maps that report histone FRET with H2B-mCherry (red pixels = FRET, teal pixels = no FRET) in MCF10A, MCF10A$^{BRCA1-KO}$ and MCF10A$^{BRCA1-KO+53BP1-KD}$ cells before and 1 hour after NCS treatment. Scale bar: 5 μm. **B.** Quantification of the fraction of pixels exhibiting histone FRET (indicative of compact chromatin) across multiple cells under the same conditions as in panel A. n ≥ 9 cells from 3 independent experiments. The box and whisker plots show the minimum, maximum and sample mean. ns P > 0.05, * P < 0.05, **** P < 0.0001, t-test. **C.** Quantification of DSB diffusion coefficients for eGFP-53BP1$_{1220–1711}$ positive DSB trajectories. In C error bars represent SEM and DSB trajectory counts from left to right are 232, 294 and 93, from n ≥ 9 cells across 3 independent experiments. ns P > 0.05, ** P < 0.01, **** P < 0.0001, one-way ANOVA. **D.** Intensity images of eGFP-53BP1$_{1220–1711}$ in DIvA$^{BRCA1-KO}$ 1 hour after 4-OHT treatment (top row), with zoomed-in images of the white boxed region showing DSB foci fusing as a function of time (bottom row). Scale bar: 5 μm. **E.** Representative mitotic spreads stained with Hoechst 33342 in MCF10A, MCF10A$^{BRCA1-KO}$ and MCF10A$^{BRCA1-KO+53BP1-KD}$ cells after 16 hours of treatment with 2 μM Olaparib. Red arrowheads indicate mis-rejoined chromosomes. Scale bar: 20 μm. **F.** Quantification of mis-rejoined chromosomes shown in panel E. In F error bars represent SEM and data are from ≥ 20 metaphase cells across 2 independent experiments. ns P > 0.05, *** P < 0.001, **** P < 0.0001, one-way ANOVA.

Discussion

In this study, we developed a multiplexed FLIM-FRET and SPT microscopy framework to directly correlate nanoscale chromatin compaction with DSB mobility at individual, genetically induced DSBs in live human cells. Using this approach, we made four key discoveries. First, DSB induction triggers global chromatin compaction while the local chromatin surrounding both NHEJ- and HR-associated DSBs remains open relative to the

surrounding nucleoplasm, establishing a compaction gradient between each DSB and the nucleus. Second, this gradient is steeper at PALB2-positive than 53BP1-positive DSBs and correlates with higher mobility at HR- versus NHEJ-associated breaks, suggesting that the broader chromatin compaction landscape contributes to the distinct mobility regimes of the two repair pathways. Third, BRCA1 and 53BP1 antagonistically regulate both the global chromatin compaction response to DSBs and DSB mobility: 53BP1 drives compaction and promotes mobility, while BRCA1 counterbalances compaction and restrains mobility, with co-depletion of both proteins restoring both readouts to baseline. Fourth, BRCA1 loss in MCF10A breast epithelial cells drives chromatin over-compaction and DSB hyper-mobility, resulting in increased chromosome mis-joining under PARP inhibitor treatment, an effect fully rescued by co-depletion of 53BP1 (*78*). Together, these findings uncover a chromatin compaction-dependent mechanism of DSB mobility control that enforces repair pathway identity and underlies PARP inhibitor sensitivity in BRCA1-deficient cells.

The correlation between chromatin compaction and DSB mobility we observe raises the question of what physical mechanism links these two properties. Previous studies have established that DSB mobility enhancement depends on 53BP1, the microtubule network, and the LINC complex, yet the specific mediator that transduces cytoskeletal forces to the nucleus remains unknown. Given the large size of the mammalian nucleus (10–20 μm in diameter) and the rarity of large-scale DSB translocation to the nuclear periphery, it is unlikely that all DSBs physically interact with the LINC complex through 53BP1. We propose two complementary mechanisms. First, the combination of global chromatin compaction and local decompaction at DSB sites may generate internal mechanical forces, analogous to a tension gradient, that drive DSB movement. This is supported by our observation that HR-associated DSBs, which exhibit faster and more extensive local decompaction, show a more rapid increase in mobility than NHEJ-associated DSBs **(Fig. 5A–B)**. A similar mechanism has been proposed in yeast cells, whereby local chromatin expansion at DSB sites promotes break extrusion (*42*). Second, global chromatin compaction may increase the stiffness of the chromatin fibre, enhancing its capacity to transmit cytoskeletal forces from the nuclear envelope to interior DSB sites (*79*). Consistent with this, 53BP1 loss impairs both global compaction and DSB mobility, while BRCA1 loss produces chromatin over-compaction and excessive mobility. Distinguishing these mechanisms will require further biophysical measurements and chromatin modelling.

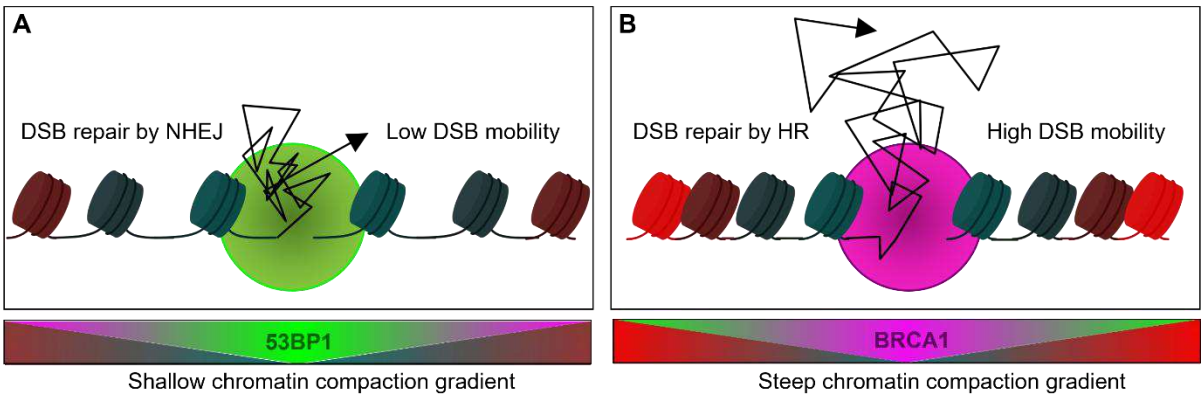


Figure 5. The NHEJ versus HR chromatin compaction gradient differentially regulates DSB mobility. DSB induction triggers global chromatin compaction while the local chromatin surrounding each break remains open relative to the surrounding nucleoplasm, establishing a compaction gradient between each DSB and the nucleus. **A.** At NHEJ-associated DSBs, where 53BP1 is abundant, this gradient is shallow and DSB mobility is restrained. **B.** At HR-associated DSBs, where BRCA1 is abundant, the gradient is steeper and DSB mobility is enhanced, expanding the nuclear search space available to the damaged locus for homology search.

The antagonistic roles of BRCA1 and 53BP1 in regulating DSB mobility extend a well-established molecular framework into the biophysical domain. While their opposing roles in DNA-end resection and repair pathway choice are well characterised, our findings reveal that this antagonism also operates at the level of chromatin structure and mobility. We show that 53BP1 promotes DSB mobility not only at NHEJ sites but also at HR sites, consistent with its known localisation at the periphery of HR repair foci (*80*), potentially facilitating the homology search by expanding the nuclear search space available to the damaged locus. Conversely, BRCA1 restrains mobility at both repair sites, likely through its known interaction with the SWI/SNF (*81*) or CBP/P300 (*82*) chromatin remodeller, which may prevent chromatin over-compaction and thereby limit excessive DSB movement. It is important to note that in the knockdown experiments reported here, we measured nuclear-wide chromatin compaction rather than the local compaction gradient at individual DSBs, since the experimental design did not combine the H2B FRET pair with repair protein markers in the same cell. Whether BRCA1 and 53BP1 differentially regulate the local compaction gradient at NHEJ versus HR sites specifically, in addition to global compaction, remains an important question for future work combining the full multiplexed FLIM-FRET and SPT framework in the knockdown backgrounds.

The functional consequence of aberrant DSB mobility in BRCA1-deficient cells provides a biophysical explanation for PARP inhibitor sensitivity(*83*). Chromatin mobility is a key determinant of DSB encounter frequency — the rate at which broken DNA ends from different chromosomal loci come into proximity, and even modest increases in mobility can substantially elevate the probability of erroneous chromosome rejoining, particularly when DSB density is high (*44, 48, 84*). PARP inhibitors generate high-density DSBs by trapping PARP at single-strand breaks, converting them to DSBs at replication forks, and our data suggest that the DSB hyper-mobility driven by BRCA1 loss dramatically increases the likelihood of mis-rejoining between these lesions, explaining the synthetic lethality between BRCA1 deficiency and PARP inhibition. The rescue of both chromatin mobility and chromosome mis-rejoining by 53BP1 co-depletion in BRCA1 KO MCF10A cells provides a direct mechanistic explanation for the clinical observation that 53BP1 loss confers PARP inhibitor resistance in BRCA1-deficient tumours. More broadly, chromatin mobility may serve as a biophysical readout that integrates multiple signalling inputs, including DSB repair proteins such as ATM and Rad51, chromatin remodellers such as the INO80 complex, and cytoskeletal components, and could potentially serve as a biomarker for predicting patient response to DSB-inducing therapies including PARP inhibitors and platinum-based chemotherapy.

Materials and methods

Cloning. H2B-eGFP and H2B-mCherry were generated in-house previously(*39*). eGFP-53BP1 (Addgene #60813), GFP-PALB2 (Addgene #71113), and mCherry-BP1-2 (Addgene #19835, named as $53BP1_{1220\text{-}1771}$ in this study)(*55*) were purchased from Addgene. To generate HaloTag fusion constructs, the coding sequences of PALB2 and 53BP1 were PCR-amplified and cloned into a HaloTag expression vector via KpnI and BamHI restriction enzyme digestion followed by ligation, generating Halo-PALB2, Halo-53BP1, and Halo-$53BP1_{1220\text{-}1771}$. To make eGFP-$53BP1_{1220\text{-}1771}$, the $53BP1_{1220\text{-}1771}$ fragment was PCR-amplified from the mCherry-53BP1-2 plasmid and subcloned into the pEGFP-C1 vector using XhoI and BamHI restriction sites followed by ligation.

Cell culture, transient transfection, immunofluorescence, and Halo tag labeling. DIvA cells (originally provided by Gaëlle Legube, LBCMCP, CNRS, Toulouse, France) were grown in Dulbecco's modified Eagle's medium (Lonza) supplemented with 10% bovine growth serum (Gibco), 1× Pen-Strep (Lonza), and 1 µg/ml puromycin (Thermo Fisher Scientific) at 37 °C in

5% CO2. MCF10A and BRCA1 knock-out MCF10A cell lines are provided by Ian Campbell, PeterMac, Melbourne, Australia), briefly bi-allelic *BRCA1* knockout was generated in MCF10A cells using CRISPR/Cas9-mediated genome editing and electroporation-based nucleofection at the Victorian Centre for Functional Genomics, Peter MacCallum Cancer Centre. The *BRCA1*-targeting sgRNA (5′-TGGGAAAACCTATCGGAAGA-3′) was designed using CRISPOR and synthesized by Integrated DNA Technologies. For each reaction, approximately 0.3 million MCF10A cells were prepared. A Cas9–sgRNA ribonucleoprotein complex containing 37 pmol of purified Cas9 nuclease and 100 pmol of sgRNA was assembled at room temperature for 10 minutes. The complex was then introduced into the cells using the 4D-Nucleofector X Unit and a pre-optimised MCF10A electroporation program('MCF7'; Lonza). Following nucleofection, the cells were incubated in pre-warmed high-serum recovery medium and allowed to recover for at least five days before clone establishment and validation. Whole-genome sequencing confirmed that the selected *BRCA1*-KO clone carried the frameshift variant *BRCA1 c.1400_1401insT, p.K467Nfs*13* (*85*).

For live-cell microscopy experiments, cells were plated 24 h before experiments onto 35 mm glass bottom dishes and transiently transfected or co-transfected with the following plasmids: eGFP-53BP1, eGFP-BP1-2, Halo-BP1-2, Halo-PALB2, Halo-53BP1, H2B-eGFP and H2B-mCherry, via use of Lipofectamine 3000 according to the manufacturer's protocol. For IF against BRCA1 (Catalogue number SAB2702136, Sigma) and 53BP1 (Catalogue number 4937S, Cell Signaling), cells were fixed with 4% paraformaldehyde for 15 min, permeabilized with 1 mg/ml Triton X-100 for 15 min at room temperature, and blocked with 1% bovine serum albumin, each in a phosphate-buffered saline buffer. Primary antibody (1: 200 dilution) was incubated overnight at 4 °C. Secondary antibody (Catalogue number A21244, Invitrogen 1: 1000) was incubated for 1 h at room temperature. For DNA staining, cells were incubated with 1 μM Hoechst 33342 for 10 min at room temperature. Halo tag was labelled with Janelia Fluor 646 (JF646, Cat. GA1120, Promega) at 100 nM final concentration for 15 minutes at 37 °C, cells were washed with phosphor buffer saline (PBS) three times prior to experiments.

Transient knockdown of 53BP1 and BRCA1 expression. siRNA-mediated knockdown of 53BP1 or BRCA1 in DIvA or MCF10A cells were achieved using Lipofectamine RNAiMAX (ThermoFisher) mediated transfection according to the manufacturer's protocol: 25 pmol of siRNA duplexes per 0.25 million cells. The sequence of the sense strand of the siRNA duplexes used 53BP1: 5′-AGAACGAGGAGACGGUAAUAGUGGG-3′(*37*) and BRCA1: 'CCCCAAGAAUGAGCUUACAAAGUGG'(*86*). Plasmids were transfected 24 h post siRNA transfection using Lipofectamine 3000. Histone FLIM-FRET or single particle tracking measurement was conducted 48 h post siRNA transfection. 53BP1 and BRCA1 knock down efficiency was validated by immunofluorescence (**Fig. S7**).

PARP inhibitor treatment and metaphase chromosome preparation. MCF10A, MCF10A$^{BRCA1\text{-}KO}$, and MCF10A$^{BRCA1\text{-}KO+53BP1\text{-}KD}$ cells were treated with 2 μM Olaparib for 16 hours before metaphase chromosome preparation (**Fig. 4**). To arrest cells in metaphase, Colcemid (KaryoMAX) was added to a final concentration of 10 μg/mL, and the cells were incubated for 2 hours at 37 °C. The cells were then harvested and subjected to hypotonic swelling in 0.075 M KCl, followed by fixation in methanol and acetic acid at a 3:1 ratio (v/v). After centrifugation at 900 × g for 5 minutes, the cell pellet was resuspended, and the suspension was dropped onto clean glass slides. The slides were air-dried and stained with DAPI.

Confocal Laser Scanning Microscopy. All microscopy measurements were performed on an Olympus FV3000 laser scanning microscope coupled to an ISS A320 Fast FLIM box for fluorescence lifetime data acquisition. A 60X water immersion objective (1.2 NA) was used

for all experiments, and the live cells were imaged at 37 degrees in 5% CO2. For acquiring single-channel time-lapse movies (**Fig. 4C-D**), eGFP tagged plasmids were excited by a solid-state laser diode operating at 488 nm, the resulting fluorescence signal directed through a 405/488/561 dichroic mirror to an internal GaAsP photomultiplier detector set to collect 500-600 nm. For acquiring dual channel time lapse movies (**Fig. 2A; Fig. 3C**), the eGFP and HaloJF646 tagged plasmids were excited by a solid-state laser diode operating at 488 nm and and 640 nm, the resulting fluorescence signal directed through a 405/488/561 dichroic mirror to two internal GaAsP photomultiplier detectors set to collect 500-540 nm and 650-750 nm. For acquiring single-channel DAPI images (**Fig. 4E**), DAPI were excited by solid-state laser diodes operating at 405 nm, and the resulting signal was directed through a 405/488/561 dichroic mirror to an internal GaAsP photomultiplier detector set to collect 430-470 nm. For immunofluorescence (IF) measurements (**Fig. S7**), Hoechst 33342 and Alexa Fluorophore (AF647) were excited by solid-state laser diodes operating at 405 nm and 640 nm, respectively, and the resulting signal was directed through a 405/488/561 dichroic mirror to two internal GaAsP photomultiplier detectors set to collect 430-470 nm and 650-750 nm, respectively.

***Microscopy data acquisition*.** Single-colour single-particle tracking (SPT) was performed to measure DNA double-strand break (DSB) mobility in MCF10A cells expressing eGFP-53BP1$_{1220\text{-}1771}$. Nuclei with suitable expression levels were selected for imaging. Time-lapse movies were acquired after cells were treated with 50 ng/ml neocarzinostatin (Merck, Cat. N9162-100µg) to induce DNA DSBs. Movies were recorded using the following settings: 108 nm pixel size, 12.5 µs pixel dwell time, 256 × 256 pixels per frame, 5 s frame interval, and 120 frames in total. For dual-colour SPT measurements, DIvA cells expressing either eGFP-53BP1 and Halo-JF646-PALB2 for **Fig. 2**, or eGFP-53BP1$_{1220\text{-}1771}$and Halo-JF646-PALB2 for **Fig. 3**, were selected for imaging. DNA DSBs were induced by adding 300 nM 4-hydroxytamoxifen (Merck, Cat. H6278-10MG). Dual-colour time-lapse movies were then acquired using the following settings: 108 nm pixel size, 12.5 µs pixel dwell time, 256 × 256 pixels per frame, and 5 s frame interval. A total of 360 frames were acquired for **Fig. 2**, and 120 frames were acquired for **Fig. 3.** Fluorescence lifetime imaging microscopy (FLIM) was used to measure the donor lifetime of H2B-eGFP in cells co-expressing the FRET acceptor H2B-mCherry(*39, 87, 88*), as shown in Figs. 1, 2, 3 and 4. Intensity images of the donor, H2B-eGFP, and acceptor, H2B-mCherry, were acquired using fixed laser power and detector gain settings, with the detector gain set to 500 V. A FLIM image was then acquired from the same nucleus and field of view in the H2B-eGFP channel only for subsequent FRET analysis. FLIM images were acquired with a 256 × 256 pixel frame size, 20 µs pixel dwell time, 108 nm pixel size, and 20-frame integration. H2B-eGFP was excited using an external pulsed 488 nm laser at 80 MHz. The emitted signal was collected using an external photomultiplier detector, H7422P-40, Hamamatsu, fitted with a 520/50 nm bandpass filter. The signal was processed using an ISS A320 FastFLIM data acquisition card, which applies digital frequency-domain analysis to calculate the fluorescence lifetime of H2B-eGFP in each pixel. For correlative SPT and histone FLIM-FRET measurements, shown in **Fig. 1**, DIvA cells expressing H2B-eGFP, H2B-mCherry, and either Halo-JF646-53BP1 or Halo-JF646-PALB2 were selected. H2B-eGFP FLIM images were first acquired as described above. This was followed by single-colour time-lapse imaging of Halo-JF646-tagged 53BP1 or PALB2. Time-lapse movies were acquired using the following settings: 108 nm pixel size, 12.5 µs pixel dwell time, 256 × 256 pixels per frame, 5 s frame interval, and 60 frames in total. The H2B-eGFP FLIM acquisition and single colour time-lapse imaging cycle was then repeated for a further 11 rounds.

FLIM-FRET Analysis. The fluorescence decay recorded in each pixel of a FLIM image was quantified by the phasor approach to lifetime analysis. Each pixel of the FLIM image gives rise to a single point (phasor) in the phasor plot, and, when used in reciprocal mode, enables each

point of the phasor pot to be mapped to each pixel of the FLIM image. Since phasors follow simple vector algebra, it is possible to determine the fractional contribution of two or more independent molecular species coexisting in the same pixel (e.g., autofluorescence and a fluorescent protein). In the case of two independent species, all possible weightings give a phasor distribution along a linear trajectory than joins the phasors of the individual species in pure form. In the case of a FRET experiment where the lifetime of the donor molecule is changed upon interaction with an acceptor molecule, the realization of all possible phasors quenched with different efficiencies describe a curved trajectory in the phasor plot. The FRET trajectory follows the classical definition of FRET efficiency. As described in previous paper, the contribution of the background (cellular auto-fluorescence) and of the donor without acceptor were evaluated by using the rule of the linear combination, with the background phasor and donor unquenched determined independently(*39, 88, 89*). In the case of $MCF10A^{H2B\text{-}2FP}$ or $DIvA^{H2B\text{-}2FP}$, the FRET efficiency varied as a function of local nucleosome proximity; thus, the trajectory of phasor clusters between the donor phasor (2.6 ns, 0% FRET) and highest FRET state (**2.1 ns, Fig. S2, S6; Fig 1-4**) represent the different states of chromatin compaction in any one pixel. By linking two phasor cursors between these two terminal phasor locations, we can pseudo-colour each pixel of a FLIM map according to the exact FRET efficiency detected at that location. Furthermore, from linking two additional cursors between the donor phasor and background phasor, we can also quantify the contribution of cellular autofluorescence in each pixel. To increase phasor accuracy, a 3 x 3 spatial median filter was applied twice to the FLIM maps presented in *Results* before FRET analysis. A 53BP1 and PALB2 intensity-based mask were used to quantify these parameters in the nucleoplasm versus within DSB foci (**Fig. 1**). All FLIM-FRET quantification was performed in the SimFCS software developed at the Laboratory for Fluorescence Dynamics (www.lfd.uci.edu) and a in house developed Matlab code published previously(*89*).

***Single particle tracking Analysis*.** Tracking of 53BP1 foci (**Fig. 4**) was performed with ImageJ software by following the protocol published by Lottersberger and colleagues(*57*). Briefly, cells were registered by the StackRegJ plugin using Rigid Body(*90*) and particles were tracked using the Mosaic Particle Detector and Tracker plugin (*74*) with the following parameters for particle detection and tracking: radius=6 pixels; cutoff=0 pixels; percentile=0.2-3; link range=3; displacement=3 pixels. The x and y coordinates of each trajectory were used for further calculation. All Halo-JF646-BP1-2 foci in a cell that were continuously tracked for at least 60 frames were analysed. For two colour time-lapse movies, two channels, eGFP-53BP1 & Halo-JF646-PALB2 (**Fig. 2**) or $eGFP\text{-}53BP1_{1220\text{-}1771}$ & Halo-JF646-PALB2 (**Fig. 3**) were registered by the StackRegJ plugin using Rigid Body simultaneously, and then the channels were split, followed by particle tracking of each channel independently as in the one colour SPT tracking setting described above. x and y coordinates of foci that were continuously tracked for 60 frames were used for mean square displacement plotting, and the generalized two-dimensional diffusion coefficients of all orders $\nu > 0$ are obtained from the y-axis intercepts y0 as: $D\nu = (2\nu)^{-1} \cdot \exp(y0)$. D2 corresponds to the regular diffusion constant in the case of strongly self-similar, pure diffusion as described previously(*74*).

Correlative single-particle tracking and histone FLIM–FRET data analysis. Twelve single-colour intensity movies, each containing 60 frames, were acquired to measure the mobility of Halo-JF646–53BP1- or Halo-JF646–PALB2-labelled DNA double-strand breaks (DSBs). The 12 movies were concatenated in ImageJ to generate a continuous 720-frame sequence for single-particle tracking analysis. Before tracking, cell movement was corrected using the StackRegJ plugin with the rigid-body transformation function. The x- and y-axis translations and rotational correction applied to each frame were exported to Excel for subsequent analysis.

53BP1- or PALB2-positive DSB foci were tracked using the Mosaic Particle Detector and Tracker plugin. The following parameters were used for particle detection and tracking: radius, 6 pixels; cutoff, 0 pixels; percentile, 0.2–3; link range, 3 frames; and maximum displacement, 3 pixels. Only foci that were continuously tracked for at least 180 frames, corresponding to a minimum of three consecutive movies, were included in subsequent analyses. The diffusion coefficient of each DSB focus was calculated separately for each 60-frame movie covered by its trajectory. For example, for a trajectory extending from frames 150 to 450, mean squared displacement (MSD) curves were calculated and fitted separately for frames 150–179, 180–239, 240–299, 300–359, 360–419, and 420–450. This approach enabled changes in the mobility of the same DSB focus to be compared across successive imaging periods. To correlate DSB mobility with local chromatin structure, the 12 histone FLIM–FRET maps generated in MATLAB were spatially aligned using the translation and rotation corrections obtained from the first frame of each corresponding intensity movie. This frame was acquired immediately after each histone FLIM–FRET measurement. For each movie, the position of a tracked DSB focus in the first available frame was used as the centre of a 6-pixel-diameter region of interest. The FRET fraction within this region was calculated to quantify the local chromatin compaction associated with that DSB. For example, for a trajectory extending from frames 150 to 450, the DSB coordinates at frames 150, 180, 240, 300, 360, and 420 were used to extract the corresponding local chromatin compaction values from the aligned FLIM–FRET maps.

Statistics and figure preparation. Statistical analysis was performed by using GraphPad Prism software. Figures were prepared by use of Adobe Illustrator, MATLAB, ImageJ, and SimFCS.

Data availability

The datasets generated during and/or analysed during the current study are available from the corresponding author on reasonable request.

Acknowledgements

E.H was supported by a Future Fellowship (FT200100401) and Jacob Haimson Beverly Mecklenburg Lectureship. This work was supported by ARC Discovery Project Grants (DP180101387 and DP21010298) and the ARC Centre of Excellence in Quantum Biotechnology (CE230100021). We thank the Biological Optical Microscopy Platform, University of Melbourne, for enabling access to the Olympus FV3000 confocal laser scanning microscope.

Contributions

J.L and E.H conceived the study and wrote the manuscript. J.L, J.S.V, S.M.C, A.G, and L.W conducted the experiments. J.L, J.S.V, S.M.C, A.N.S, and E.H analysed the data. X.Z, Q.Z, I.G.C created and provided unique reagents.

References

1. K. Crasta *et al.*, DNA breaks and chromosome pulverization from errors in mitosis. *Nature* **482**, 53-58 (2012).
2. K. Karanam, R. Kafri, A. Loewer, G. Lahav, Quantitative live cell imaging reveals a gradual shift between DNA repair mechanisms and a maximal use of HR in mid S phase. *Mol Cell* **47**, 320-329 (2012).
3. J. R. Chapman, M. R. Taylor, S. J. Boulton, Playing the end game: DNA double-strand break repair pathway choice. *Mol Cell* **47**, 497-510 (2012).

4. C. Escribano-Diaz *et al.*, A cell cycle-dependent regulatory circuit composed of 53BP1-RIF1 and BRCA1-CtIP controls DNA repair pathway choice. *Mol Cell* **49**, 872-883 (2013).
5. S. C. Kowalczykowski, An Overview of the Molecular Mechanisms of Recombinational DNA Repair. *Cold Spring Harb Perspect Biol* **7**, (2015).
6. M. Zimmermann, T. de Lange, 53BP1: pro choice in DNA repair. *Trends Cell Biol* **24**, 108-117 (2014).
7. S. F. Bunting *et al.*, 53BP1 inhibits homologous recombination in Brca1-deficient cells by blocking resection of DNA breaks. *Cell* **141**, 243-254 (2010).
8. A. Fradet-Turcotte *et al.*, 53BP1 is a reader of the DNA-damage-induced H2A Lys 15 ubiquitin mark. *Nature* **499**, 50-54 (2013).
9. S. Panier, S. J. Boulton, Double-strand break repair: 53BP1 comes into focus. *Nat Rev Mol Cell Biol* **15**, 7-18 (2014).
10. R. M. Densham, J. R. Morris, Moving Mountains-The BRCA1 Promotion of DNA Resection. *Front Mol Biosci* **6**, 79 (2019).
11. C. C. Chen, W. Feng, P. X. Lim, E. M. Kass, M. Jasin, Homology-Directed Repair and the Role of BRCA1, BRCA2, and Related Proteins in Genome Integrity and Cancer. *Annu Rev Cancer Biol* **2**, 313-336 (2018).
12. O. Zgheib, K. Pataky, J. Brugger, T. D. Halazonetis, An oligomerized 53BP1 tudor domain suffices for recognition of DNA double-strand breaks. *Mol Cell Biol* **29**, 1050-1058 (2009).
13. O. Zgheib *et al.*, ATM signaling and 53BP1. *Radiother Oncol* **76**, 119-122 (2005).
14. Y. Huyen *et al.*, Methylated lysine 79 of histone H3 targets 53BP1 to DNA double-strand breaks. *Nature* **432**, 406-411 (2004).
15. L. B. Schultz, N. H. Chehab, A. Malikzay, T. D. Halazonetis, p53 binding protein 1 (53BP1) is an early participant in the cellular response to DNA double-strand breaks. *J Cell Biol* **151**, 1381-1390 (2000).
16. M. A. Ricci, C. Manzo, M. F. Garcia-Parajo, M. Lakadamyali, M. P. Cosma, Chromatin fibers are formed by heterogeneous groups of nucleosomes in vivo. *Cell* **160**, 1145-1158 (2015).
17. Z. Chen, J. K. Tyler, The Chromatin Landscape Channels DNA Double-Strand Breaks to Distinct Repair Pathways. *Front Cell Dev Biol* **10**, 909696 (2022).
18. A. Kalousi, E. Soutoglou, Nuclear compartmentalization of DNA repair. *Curr Opin Genet Dev* **37**, 148-157 (2016).
19. Z. Mirman, T. de Lange, 53BP1: a DSB escort. *Genes Dev* **34**, 7-23 (2020).
20. G. Soria, S. E. Polo, G. Almouzni, Prime, repair, restore: the active role of chromatin in the DNA damage response. *Mol Cell* **46**, 722-734 (2012).
21. A. Marin-Gonzalez *et al.*, Cohesin drives chromatin scanning during the RAD51-mediated homology search. *Science* **390**, eadw1928 (2025).
22. M. A. E. van Bueren, A. Janssen, The impact of chromatin on double-strand break repair: Imaging tools and discoveries. *DNA Repair (Amst)* **133**, 103592 (2024).
23. C. Mohan, C. Das, J. Tyler, Histone and Chromatin Dynamics Facilitating DNA repair. *DNA Repair (Amst)* **107**, 103183 (2021).
24. B. D. Price, A. D. D'Andrea, Chromatin remodeling at DNA double-strand breaks. *Cell* **152**, 1344-1354 (2013).
25. S. E. Polo, Reshaping chromatin after DNA damage: the choreography of histone proteins. *J Mol Biol* **427**, 626-636 (2015).

26. M. K. Ayrapetov, O. Gursoy-Yuzugullu, C. Xu, Y. Xu, B. D. Price, DNA double-strand breaks promote methylation of histone H3 on lysine 9 and transient formation of repressive chromatin. *Proc Natl Acad Sci U S A* **111**, 9169-9174 (2014).
27. C. Baldeyron, G. Soria, D. Roche, A. J. Cook, G. Almouzni, HP1alpha recruitment to DNA damage by p150CAF-1 promotes homologous recombination repair. *J Cell Biol* **193**, 81-95 (2011).
28. J. Bewersdorf, B. T. Bennett, K. L. Knight, H2AX chromatin structures and their response to DNA damage revealed by 4Pi microscopy. *Proc Natl Acad Sci U S A* **103**, 18137-18142 (2006).
29. M. Mikhova *et al.*, Single-molecule imaging reveals the kinetics of non-homologous end-joining in living cells. *Nat Commun* **15**, 10159 (2024).
30. R. C. Burgess, B. Burman, M. J. Kruhlak, T. Misteli, Activation of DNA damage response signaling by condensed chromatin. *Cell Rep* **9**, 1703-1717 (2014).
31. S. Khurana *et al.*, A macrohistone variant links dynamic chromatin compaction to BRCA1-dependent genome maintenance. *Cell Rep* **8**, 1049-1062 (2014).
32. M. J. Kruhlak *et al.*, Changes in chromatin structure and mobility in living cells at sites of DNA double-strand breaks. *J Cell Biol* **172**, 823-834 (2006).
33. H. Sellou *et al.*, The poly(ADP-ribose)-dependent chromatin remodeler Alc1 induces local chromatin relaxation upon DNA damage. *Mol Biol Cell* **27**, 3791-3799 (2016).
34. G. Smeenk *et al.*, Poly(ADP-ribosyl)ation links the chromatin remodeler SMARCA5/SNF2H to RNF168-dependent DNA damage signaling. *J Cell Sci* **126**, 889-903 (2013).
35. H. Strickfaden *et al.*, Poly(ADP-ribosyl)ation-dependent Transient Chromatin Decondensation and Histone Displacement following Laser Microirradiation. *J Biol Chem* **291**, 1789-1802 (2016).
36. E. Hinde, X. Kong, K. Yokomori, E. Gratton, Chromatin dynamics during DNA repair revealed by pair correlation analysis of molecular flow in the nucleus. *Biophys J* **107**, 55-65 (2014).
37. J. Lou, D. G. Priest, A. Solano, A. Kerjouan, E. Hinde, Spatiotemporal dynamics of 53BP1 dimer recruitment to a DNA double strand break. *Nat Commun* **11**, 5776 (2020).
38. A. Quessada-Vial, A. M. van Oijen, How DNA-repair proteins find their targets. *Proc Natl Acad Sci U S A* **109**, 18243-18244 (2012).
39. J. Lou *et al.*, Phasor histone FLIM-FRET microscopy quantifies spatiotemporal rearrangement of chromatin architecture during the DNA damage response. *Proc Natl Acad Sci U S A* **116**, 7323-7332 (2019).
40. J. Lou, A. Solano, Z. Liang, E. Hinde, Phasor Histone FLIM-FRET Microscopy Maps Nuclear-Wide Nanoscale Chromatin Architecture With Respect to Genetically Induced DNA Double-Strand Breaks. *Front Genet* **12**, 770081 (2021).
41. F. Ochs *et al.*, Stabilization of chromatin topology safeguards genome integrity. *Nature* **574**, 571-574 (2019).
42. A. Amitai, A. Seeber, S. M. Gasser, D. Holcman, Visualization of Chromatin Decompaction and Break Site Extrusion as Predicted by Statistical Polymer Modeling of Single-Locus Trajectories. *Cell Rep* **18**, 1200-1214 (2017).
43. H. Bordelet, K. Dubrana, Keep moving and stay in a good shape to find your homologous recombination partner. *Curr Genet* **65**, 29-39 (2019).

44. V. Dion, S. M. Gasser, Chromatin movement in the maintenance of genome stability. *Cell* **152**, 1355-1364 (2013).
45. R. Oshidari, K. Mekhail, A. Seeber, Mobility and Repair of Damaged DNA: Random or Directed? *Trends Cell Biol* **30**, 144-156 (2020).
46. M. J. Smith, R. Rothstein, Poetry in motion: Increased chromosomal mobility after DNA damage. *DNA Repair (Amst)* **56**, 102-108 (2017).
47. C. Zimmer, E. Fabre, Chromatin mobility upon DNA damage: state of the art and remaining questions. *Curr Genet* **65**, 1-9 (2019).
48. A. Seeber, M. H. Hauer, S. M. Gasser, Chromosome Dynamics in Response to DNA Damage. *Annu Rev Genet* **52**, 295-319 (2018).
49. E. Soutoglou *et al.*, Positional stability of single double-strand breaks in mammalian cells. *Nat Cell Biol* **9**, 675-682 (2007).
50. J. A. Aten *et al.*, Dynamics of DNA double-strand breaks revealed by clustering of damaged chromosome domains. *Science* **303**, 92-95 (2004).
51. J. Mine-Hattab, R. Rothstein, Increased chromosome mobility facilitates homology search during recombination. *Nat Cell Biol* **14**, 510-517 (2012).
52. V. Dion, V. Kalck, C. Horigome, B. D. Towbin, S. M. Gasser, Increased mobility of double-strand breaks requires Mec1, Rad9 and the homologous recombination machinery. *Nat Cell Biol* **14**, 502-509 (2012).
53. C. Lemaitre, E. Soutoglou, DSB (Im)mobility and DNA repair compartmentalization in mammalian cells. *J Mol Biol* **427**, 652-658 (2015).
54. P. M. Krawczyk *et al.*, Chromatin mobility is increased at sites of DNA double-strand breaks. *J Cell Sci* **125**, 2127-2133 (2012).
55. N. Dimitrova, Y. C. Chen, D. L. Spector, T. de Lange, 53BP1 promotes non-homologous end joining of telomeres by increasing chromatin mobility. *Nature* **456**, 524-528 (2008).
56. K. S. Lawrence *et al.*, LINC complexes promote homologous recombination in part through inhibition of nonhomologous end joining. *J Cell Biol* **215**, 801-821 (2016).
57. F. Lottersberger, R. A. Karssemeijer, N. Dimitrova, T. de Lange, 53BP1 and the LINC Complex Promote Microtubule-Dependent DSB Mobility and DNA Repair. *Cell* **163**, 880-893 (2015).
58. H. Saad *et al.*, DNA dynamics during early double-strand break processing revealed by non-intrusive imaging of living cells. *PLoS Genet* **10**, e1004187 (2014).
59. B. Chen *et al.*, Dynamic imaging of genomic loci in living human cells by an optimized CRISPR/Cas system. *Cell* **155**, 1479-1491 (2013).
60. A. Becker, M. Durante, G. Taucher-Scholz, B. Jakob, ATM alters the otherwise robust chromatin mobility at sites of DNA double-strand breaks (DSBs) in human cells. *PLoS One* **9**, e92640 (2014).
61. N. W. Cho, R. L. Dilley, M. A. Lampson, R. A. Greenberg, Interchromosomal homology searches drive directional ALT telomere movement and synapsis. *Cell* **159**, 108-121 (2014).
62. V. Dion, V. Kalck, A. Seeber, T. Schleker, S. M. Gasser, Cohesin and the nucleolus constrain the mobility of spontaneous repair foci. *EMBO Rep* **14**, 984-991 (2013).
63. F. Lottersberger, A. Bothmer, D. F. Robbiani, M. C. Nussenzweig, T. de Lange, Role of 53BP1 oligomerization in regulating double-strand break repair. *Proc Natl Acad Sci U S A* **110**, 2146-2151 (2013).

64. M. J. Smith, E. E. Bryant, R. Rothstein, Increased chromosomal mobility after DNA damage is controlled by interactions between the recombination machinery and the checkpoint. *Genes Dev* **32**, 1242-1251 (2018).
65. F. R. Neumann *et al.*, Targeted INO80 enhances subnuclear chromatin movement and ectopic homologous recombination. *Genes Dev* **26**, 369-383 (2012).
66. C. Horigome *et al.*, SWR1 and INO80 chromatin remodelers contribute to DNA double-strand break perinuclear anchorage site choice. *Mol Cell* **55**, 626-639 (2014).
67. A. Seeber, V. Dion, S. M. Gasser, Checkpoint kinases and the INO80 nucleosome remodeling complex enhance global chromatin mobility in response to DNA damage. *Genes Dev* **27**, 1999-2008 (2013).
68. J. Strecker *et al.*, DNA damage signalling targets the kinetochore to promote chromatin mobility. *Nat Cell Biol* **18**, 281-290 (2016).
69. D. K. Chung *et al.*, Perinuclear tethers license telomeric DSBs for a broad kinesin- and NPC-dependent DNA repair process. *Nat Commun* **6**, 7742 (2015).
70. B. R. Schrank *et al.*, Nuclear ARP2/3 drives DNA break clustering for homology-directed repair. *Nature* **559**, 61-66 (2018).
71. R. K. Swartz, E. C. Rodriguez, M. C. King, A role for nuclear envelope-bridging complexes in homology-directed repair. *Mol Biol Cell* **25**, 2461-2471 (2014).
72. J. S. Iacovoni *et al.*, High-resolution profiling of gammaH2AX around DNA double strand breaks in the mammalian genome. *EMBO J* **29**, 1446-1457 (2010).
73. L. Massip, P. Caron, J. S. Iacovoni, D. Trouche, G. Legube, Deciphering the chromatin landscape induced around DNA double strand breaks. *Cell Cycle* **9**, 2963-2972 (2010).
74. I. F. Sbalzarini, P. Koumoutsakos, Feature point tracking and trajectory analysis for video imaging in cell biology. *J Struct Biol* **151**, 182-195 (2005).
75. S. Simhadri *et al.*, PALB2 connects BRCA1 and BRCA2 in the G2/M checkpoint response. *Oncogene* **38**, 1585-1596 (2019).
76. F. Song *et al.*, Antiparallel Coiled-Coil Interactions Mediate the Homodimerization of the DNA Damage-Repair Protein PALB2. *Biochemistry* **57**, 6581-6591 (2018).
77. Q. Ye *et al.*, BRCA1-induced large-scale chromatin unfolding and allele-specific effects of cancer-predisposing mutations. *J Cell Biol* **155**, 911-921 (2001).
78. J. M. Whalen, J. Earley, C. Silva, A. M. Mercurio, S. B. Cantor, Targeting BRCA1-deficient PARP inhibitor-resistant cells with nickases reveals nick resection as a cancer vulnerability. *Nat Cancer* **6**, 278-291 (2025).
79. G. Bastianello *et al.*, Cell stretching activates an ATM mechano-transduction pathway that remodels cytoskeleton and chromatin. *Cell Rep* **42**, 113555 (2023).
80. D. R. Whelan, E. Rothenberg, Super-resolution mapping of cellular double-strand break resection complexes during homologous recombination. *Proc Natl Acad Sci U S A* **118**, (2021).
81. D. A. Bochar *et al.*, BRCA1 is associated with a human SWI/SNF-related complex: linking chromatin remodeling to breast cancer. *Cell* **102**, 257-265 (2000).
82. G. M. Pao, R. Janknecht, H. Ruffner, T. Hunter, I. M. Verma, CBP/p300 interact with and function as transcriptional coactivators of BRCA1. *Proc Natl Acad Sci U S A* **97**, 1020-1025 (2000).
83. J. Mahadevan *et al.*, Dynamics of endogenous PARP1 and PARP2 during DNA damage revealed by live-cell single-molecule imaging. *iScience* **26**, 105779 (2023).

84. M. H. Hauer, S. M. Gasser, Chromatin and nucleosome dynamics in DNA damage and repair. *Genes Dev* **31**, 2204-2221 (2017).
85. Q. Zhao *et al.*, Investigating the contribution of rare non-coding variants in BRCA1, BRCA2 and PALB2 to hereditary breast cancer. *NPJ Breast Cancer* **12**, (2026).
86. S. M. Noordermeer *et al.*, The shieldin complex mediates 53BP1-dependent DNA repair. *Nature* **560**, 117-121 (2018).
87. D. Lleres, J. James, S. Swift, D. G. Norman, A. I. Lamond, Quantitative analysis of chromatin compaction in living cells using FLIM-FRET. *J Cell Biol* **187**, 481-496 (2009).
88. Z. Liang, J. Lou, L. Scipioni, E. Gratton, E. Hinde, Quantifying nuclear wide chromatin compaction by phasor analysis of histone Forster resonance energy transfer (FRET) in frequency domain fluorescence lifetime imaging microscopy (FLIM) data. *Data Brief* **30**, 105401 (2020).
89. Z. Liang, A. Solano, J. Lou, E. Hinde, Histone FRET reports the spatial heterogeneity in nanoscale chromatin architecture that is imparted by the epigenetic landscape at the level of single foci in an intact cell nucleus. *Chromosoma* **133**, 5-14 (2024).
90. P. Thevenaz, U. E. Ruttimann, M. Unser, A pyramid approach to subpixel registration based on intensity. *IEEE Trans Image Process* **7**, 27-41 (1998).

Supplementary Files

This is a list of supplementary files associated with this preprint. Click to download.

- Louetalsupplementaryinformation04082026.docx